Carbon 214 (2023) 118339

Contents lists available at ScienceDirect

Carbon

journal homepage: www.elsevier.com/locate/carbon

Site-specific optical encryption via nanoscale integration of carbon on monolayer WS_2

Deepa Thakur [a], Pawan Kumar [b,c,d], Arjun Barwal [e], Deep Jariwala [b], Erich Stach [c], Viswanath Balakrishnan [a,*]

[a] School of Mechanical and Materials Engineering, Indian Institute of Technology, Mandi, Himachal Pradesh, 175075, India
[b] Department of Electrical and Systems Engineering, University of Pennsylvania, Philadelphia, PA, 19104, USA
[c] Department of Material Science and Engineering, University of Pennsylvania, Philadelphia, PA, 19104, USA
[d] IMEC-Leuven, Leuven, 3001, Belgium
[e] Advanced Materials Research Centre, Indian Institute of Technology, Mandi, Himachal Pradesh, 175075, India

ARTICLE INFO

Keywords:
Data encryption
2D materials
Carbon nanostructures
Photoluminescence engineering
Electron-beam-induced deposition

ABSTRACT

The ability to selectively tune the optical properties of two-dimensional (2D) materials at specific sites is of great interest for the development of optoelectronic and photonic devices. We report site-specific electron-beam (e-beam) induced deposition for creating patterned carbon nanostructures on atomically thin 2D materials such as WS_2 and MoS_2. Various patterns ranging from microns to nanometres in size have been produced and controlled by adjusting e-beam parameters such as accelerating voltage, spot size, magnification, and irradiation time. The ultimate pattern dimensions of ~52 nm in width and ~2.58 nm in height is achieved. The patterned areas exhibit a quenching of fluorescence intensity of about three times, making it simple to identify the created structure from the 2D materials. Moreover, Kelvin probe force microscopy measurements indicated that the surface potential of the patterned sites is roughly 95.6 mV different from that of non-patterned WS_2. Finally, we have demonstrated optical encryption by selectively integrating carbon structures to modulate the optical emission of WS_2.

1. Introduction

Semiconducting transition metal dichalcogenides (TMDCs) have attracted a significant amount of research interest owing to their superior properties for a wide range of applications such as electronics, catalysis, magnetic and optical devices [1–5]. Tungsten Disulfide (WS_2) exhibit a direct bandgap in the visible range in their monolayer form with a superior quantum yield of ~6%, which makes it a very promising candidate for optical and optoelectronic applications [6,7]. Site-specific patterning based on photoluminescence (PL) engineering is suitable for the optical encoding of encrypted information [8]. PL patterning can be achieved through either enhancing or quenching the PL emission in specific regions. Various methods have been explored for PL enhancement, including oxygen adsorption [9], plasmonic nanostructures [10–12], heterostructure formation [13,14], and N_2 plasma treatment [15]. In contrast, PL quenching has been achieved using techniques such as Ga ion irradiation [16], decoration of Si nanoparticles [17], and band gap tuning [18]. However, most of these reported methods lack the ability to achieve site-specific control, and their effects can be observed across the entire sample.

Site-specific tuning of the optical emission of 2D materials by incorporating hydrocarbon or carbon (C) is a fascinating approach with the aid of intrinsic defects. For example, the commonly observed intrinsic defects in 2D materials, primarily chalcogen (S) vacancies have been shown to act as binding sites for atmospheric hydrocarbons (CHx) [19–21]. However, achieving site-specific decoration and patterning of 2D materials is highly challenging yet holds potential for tuning the properties of TMDCs. Various nanofabrication methods, such as electron-beam (e-beam) lithography, LASER patterning, He-ion beam lithography, and ice-lithography, have been used to obtain nanoscale patterns. LASER patterning offers the advantage of easy writing on a large area but suffers from poor resolution in the microns to hundreds of nanometres range [22]. He-ion lithography can achieve sub-10 nm resolution, but its low yield and high instrumentation cost limit its use [23]. E-beam lithography is a well-known lithography route, but it requires multiple processing steps with the use of various e-beam resists, etchants, and other chemicals [24]. A novel e-beam lithography technique called ice lithography uses ice instead of e-beam resist and has

* Corresponding author.
E-mail address: viswa@iitmandi.ac.in (V. Balakrishnan).

https://doi.org/10.1016/j.carbon.2023.118339
Received 24 May 2023; Received in revised form 26 July 2023; Accepted 27 July 2023
Available online 1 August 2023

demonstrated that a focused and optimized dose of e-beam can directly pattern thin films [25,26]. The utilization of e-beam technology is a highly effective approach for patterning materials, owing to its remarkable capacity to converge at the nanoscale level. Unlike traditional methods, direct e-beam patterning offers a clean and effective approach that can be used for tuning the optical properties of 2D materials for emerging applications such as optoelectronics and nanophotonics. Such precise patterning of 2D materials with the ability to tune optical properties would be also useful for encryption which has emerged as a popular and effective means of protecting privacy, by using cryptography to embed confidential data within an information medium. Luminescence, due to its direct visibility, is considered an ideal technology for encryption and decryption [8,27]. Among the various luminescent encryption technologies, PL is widely used due to its high efficiency and ease of implementation. For an encryption method to be considered effective, certain desirable aspects such as writing speed, high-security level, visual decryption for reading, erasing capability, and high spatial resolution, etc. need to be fulfilled.

In this study, we have demonstrated nanoscale site-specific patterning of C nanostructures on 2D-TMDCs (WS_2 and MoS_2) using a direct e-beam induced deposition (EBID) for optical data encryption. No e-beam resist coating was applied, resulting in a clean heterostructure interface. We have observed a strong interaction and charge transfer between the C-based nanostructures and WS_2 monolayer which can modify the optical emission and could be used for the secure transmission of sensitive information.

2. Experimental section

2.1. Material growth

The WS_2 monolayers were synthesized on a SiO_2-coated Si substrate using atmospheric pressure-chemical vapor deposition (APCVD). The pre-cleaning procedures and growth process were performed following the previously reported method [28]. In brief, dropcasted WO_3 was sulfurized at 850 °C for 10 min using pure S powder (400 mg). The precursors were transported using a gas mixture of 100 SCCM of Ar + H_2 (95% + 5%) [29]. The MoS_2 flakes were grown on a clean SiO_2/Si substrate by sulfurizing 2 mg MoO_3 powder at 650 °C for 7 min. S powder (400 mg) kept at 200 °C was transported using 20 SCCM of Ar gas [14].

2.2. Characterizations

The APCVD system utilized in this study was manufactured by Thermo Scientific. A field emission scanning electron microscope (FESEM, NANO Nova SEM 450 from FEI, USA) was employed for imaging and pattern creation. The quality of the grown material was analyzed using Raman and PL measurements performed with a 532 nm LASER and 100X objective on a LabRAM HR evolution system from Horiba Jobin Vyon. Atomic force microscopy (AFM) and Kelvin probe force microscopy (KPFM) were carried out in tapping mode configuration at a scan rate of 0.7 Hz using a Dimension Icon system from Bruker (USA). The size and morphology of the APCVD-grown 2D nanostructure were examined with the aid of a Nikon LV 100 N Pol visible light microscope (Japan). Fluorescence imaging was performed on Nikon-FN1 and Nikon-DTGTTAL SrGHT microscopes. Transmission electron microscope (TEM) investigation was performed in Tecnai G2 20 S-TWIN, FEI, USA at IIT Mandi. Scanning transmission electron microscope (STEM) and electron energy loss spectroscopy (EELS) measurements were performed using a JEOL-NEOARM microscope operated at 200 kV. Probe corrected (Cs correction) microscope uses 1 Å probe size, 4 cm, and 2 cm camera length for the HAADF-STEM and EELS measurements respectively. For STEM investigation, the samples grown using APCVD were transferred onto a quantifoil grid via a wet chemical method as described in the supplementary information.

3. Results and discussion

E-beam can be used to deposit as well as remove material depending upon the energy of e-beam used [30]. It is well-known that high-energy e-beam in the range of 80 keV–200 keV, can potentially damage samples. However, researchers have effectively utilized this process to create vacancies and voids in MoS_2, WS_2, and graphene, etc by exposing them to such high-energy e-beam. For example, Jun Chen et al. utilized e-beam (80 keV) to fabricate nanowells in bilayer WS_2 inside a scanning transmission electron microscope (STEM) [31]. In our study, we employed a low-energy e-beam (10 keV and below) with an accelerating voltage of ~10 kV, which is commonly used for specimen imaging in FESEM. Within this lower energy range, WS_2 samples are generally not susceptible to damage. Fig. 1a shows the effect of e-beam to deposit and remove the material at low and high energies. To achieve site specific patterning over WS_2 monolayers, an APCVD-grown sample over SiO_2/Si substrate was subjected to direct e-beam scanning inside a FESEM at a vacuum of ~10^{-3} Pa. Unlike conventional e-beam lithography, no resist coating was used in this process. A monolayer WS_2 flake was chosen for patterning, where the area of the desired shape and number of points were selected, similar to a regular EBID process [32]. Using this patterning process, a variety of shapes and sizes can be designed. Three exemplary patterning experiments are depicted in Fig. 1b and 1c in which a cartoon face, the letters "IIT" and a controlled dot pattern on the alternate edges of a truncated triangle are produced on a monolayer WS_2 by utilizing an e-beam. The brighter appearance observed at the edges of patterns in FESEM images can be potentially attributed to an edge effect that occurs during the imaging process. Additionally, this process is reproducible on various substrates, as illustrated in Supplementary Fig. S1.

The use of e-beam irradiation can have several effects on the material, including atomic distortion, heating, sputtering, and electrostatic charging [33,34]. To understand the precise changes that occurred in the patterned region, AFM analysis was conducted. WS_2 flake with an "IIT" pattern was imaged using AFM (Fig. 1d), and an AFM height profile was obtained along the marked red line (inset). From AFM analysis, it is evident that the height of the patterned region is ~43.8 nm higher than that of the non-patterned WS_2. This indicates that the patterning process is additive with the possibility to create various structures by adjusting the e-beam dose. It may be noted that in the AFM image (Fig. 1d) outside the flakes, the observed dot like features are particles of WS_2 that were grown during the CVD process. Another AFM image is shown in Fig. 1e to show smallest achieved patterns. In the pattered region, the smallest feature size achieved is ~52 nm in width and ~2.6 nm in height as shown in Fig. 1e along with the corresponding height profile (Fig. 1f). The patterning process was conducted using a magnification of 50000X, with 10 kV accelerating voltage, a spot size of 3, a dwell time of 30 s, and a chosen area of 3X3 μm^2. The corresponding low-mag image of this region is shown in supplementary Fig. S9.

Some of the key components of the EBID process are substrate-precursor interaction, electron-substrate interaction, and electron-precursor molecule interaction. It is known that multiple organic and inorganic species present inside the FESEM chamber and/or adsorbed on sample surface can act as a precursor for EBID [35,36]. In the EBID experiment, a beam of primary electrons is directed at the specific locations of the WS_2 monolayer with adsorbed organic species (hydrocarbons). Due to the e-beam interaction, the precursor molecules dissociate into non-volatile components and adhere to the substrate. Previous studies indicate that low-energy secondary electrons are more relevant for the deposition process [32,37]. In the present case, hydrocarbons adsorbed on WS_2 monolayer as well as hydrocarbons inside FESEM chamber act as a precursor for EBID. To gain insights into the e-beam deposited nanostructures, various microscopic and spectroscopic investigations were conducted. Specifically, FESEM elemental mapping was performed to confirm the composition of the deposited material as shown in Supplementary Fig. S2a. The results revealed that

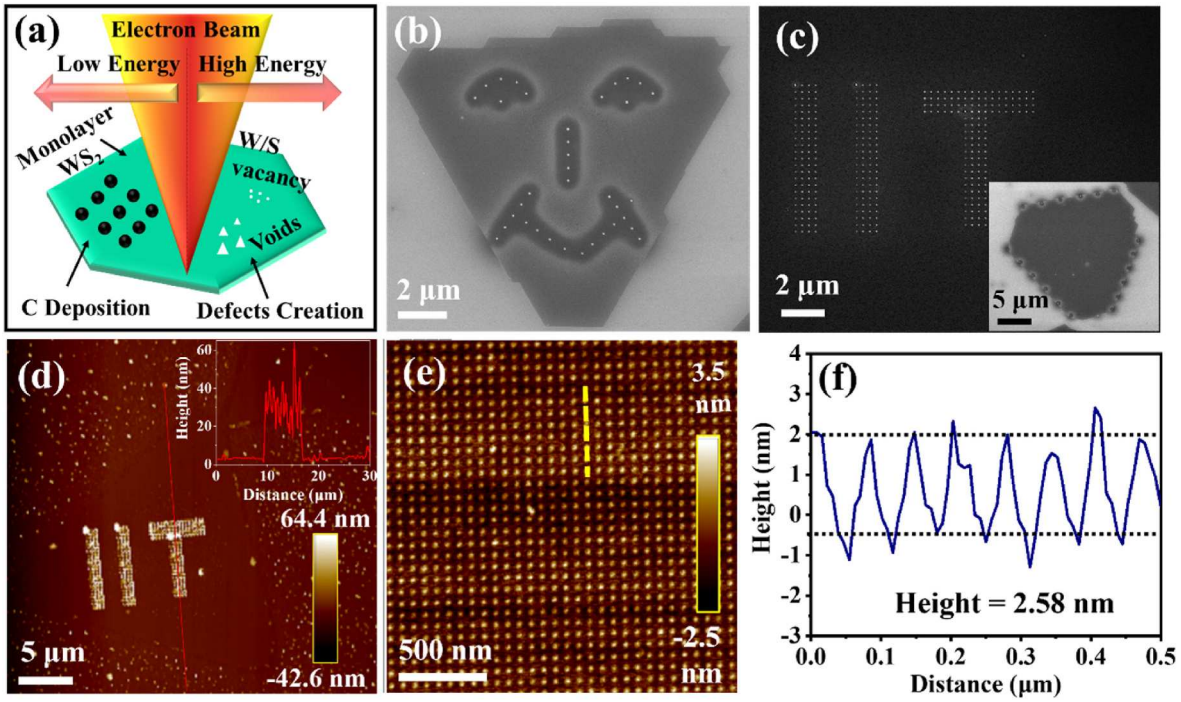

Fig. 1. (a) The schematic showing interaction of e-beam with WS_2. (b-c) E-beam patterning demonstrating various design on WS_2 monolayer. (d) AFM height image to show that patterning is an additive process. The AFM height plot is shown in inset. (e) Another AFM image to show the capability of nanoscale patterning and (f) its corresponding height plot. The measured average height of the pattern is ~2.58 nm. (A colour version of this figure can be viewed online.)

the primary element forming the dot square pattern is a C (Fig. S2b) while the presence of Tungsten (W) and Sulfur (S) are observed throughout the selected region in WS_2 monolayer (Figs. S2c and S2d). To ensure the reproducibility of the pattern method, the procedure was repeated on several different samples and also using another FESEM instrument (Carl, Zeiss, C4DFED), and similar results were obtained (Supplementary Fig. S3). The TEM bright field images of the patterned region along with the selected area electron diffraction (SAED) pattern are shown in Supplementary Fig. S4. The SAED pattern shows the hexagonal symmetry of WS_2 along with diffused ring pattern arising from amorphous C.

Fig. 2a displays a low-magnification STEM image of single C spot (bright) from the patterned region on the monolayer WS_2 (dark). Furthermore, a high-resolution atomic scale imaging was performed on the marked red region, as shown in Fig. 2b, where the atomic arrangement of WS_2 can be observed. In order to eliminate any contamination arising from sample preparation and transfer for STEM study, the sample was heated at a temperature of 300 °C for 30 min. The STEM imaging after annealing can be seen in Supplementary Fig. S5. Fig. 2c presents a high-resolution atomic scale STEM-HAADF image for the WS_2 region, recorded away from the C pattern. The low magnification image of region is presented in Supplementary Fig. S5a. To gather more information from the region, electron energy loss spectroscopy (EELS) was conducted, and the EELS plot obtained from the pattern region is presented in Fig. 2d. The obtained EELS was compared with earlier literature, and it resembles amorphous C, with the initial peak for the amorphous C k edge due to the transition to π^* molecular orbitals found at around ~286 eV [38]. Following this is a second broad peak arising from the transition to σ* orbitals [39]. The shape of the EELS plot looks similar to sp^3 and sp^2 rich C [40]. To confirm the qualitative composition of the region shown in Fig. 2e, tungsten (W) and sulfur (S) elemental scans were performed and are displayed in Fig. 2f and 2g. Additionally, Fig. 2h presents the C mapping, which confirms further C deposition in the patterned region. The STEM analysis at the interface of C and WS_2 is presented in Fig. 2i which shows C rich region (left) and C poor region (right). Three specific regions which are marked in different coloured square boxes were chosen and their corresponding Fast Fourier Transform (FFT) patterns are shown alongside in Fig. 2j–l. In FFT patterns, only hexagonal feature from WS_2 monolayer is consistently visible in all the areas. There is no sign of crystalline C-formation in the FFT diffraction pattern at any position. Among the three marked regions, the region marked in orange square correspond to C rich region while the purple square is WS_2 rich/C poor. The green coloured square at the centre refers to the C-WS_2 interface region and magnified version of the same is also presented in Fig. 2m (green square). The contrast of the W atoms towards the left side is much brighter as compared to right side. This may be due to the presence of higher thickness of C pattern along with W atoms together in the same position (top and bottom). The additive mass-thickness contrast might have resulted in higher brightness in the STEM image. Imaging the atoms of carbon up to atomic resolution is difficult due to the thick amorphous nature of C pattern on WS_2. However, in the case of WS_2, we were able to successfully capture a STEM image near the interface. Notably, no metal vacancies in the WS_2 were observed in this region which clearly suggests the non-damaging (at least for metals) character of EBID methodology to generate a C-pattern.

To further support the aforementioned claim, Raman investigation was conducted (Fig. 3a), which revealed clear signatures of the vibration modes of WS_2, i.e., 2LA(M), E' (Γ) and A_1' (Γ), in both patterned and non-patterned regions [41,42]. The E′ mode represents the in-plane vibration of WS_2, while 2LA(M) denotes the second-order longitudinal acoustic vibration mode of WS_2. These two modes are closely located in terms of their positions. Consequently, it is common for the E′ mode to appear merged with 2LA(M). Fig. 3b shows the Raman spectra of the region which is marked in Fig. 3a to clearly visualize WS_2 vibration modes {2LA(M), E' (Γ)}. The prominent peak corresponding to 2LA(M) and E′ is clearly indicated in Fig. 3b, and the position values are nearly identical considering the fact that the spectral resolution of the used Raman spectroscopy is around 0.3 cm^{-1}. At the patterned site, these modes were observed at ~350.12 cm^{-1}, 356.15 cm^{-1}, and ~416.43 cm^{-1} respectively, while in the patterned region, they appeared at ~350.30 cm^{-1}, 356.34 cm^{-1}, and ~416.75 cm^{-1}. In addition, a

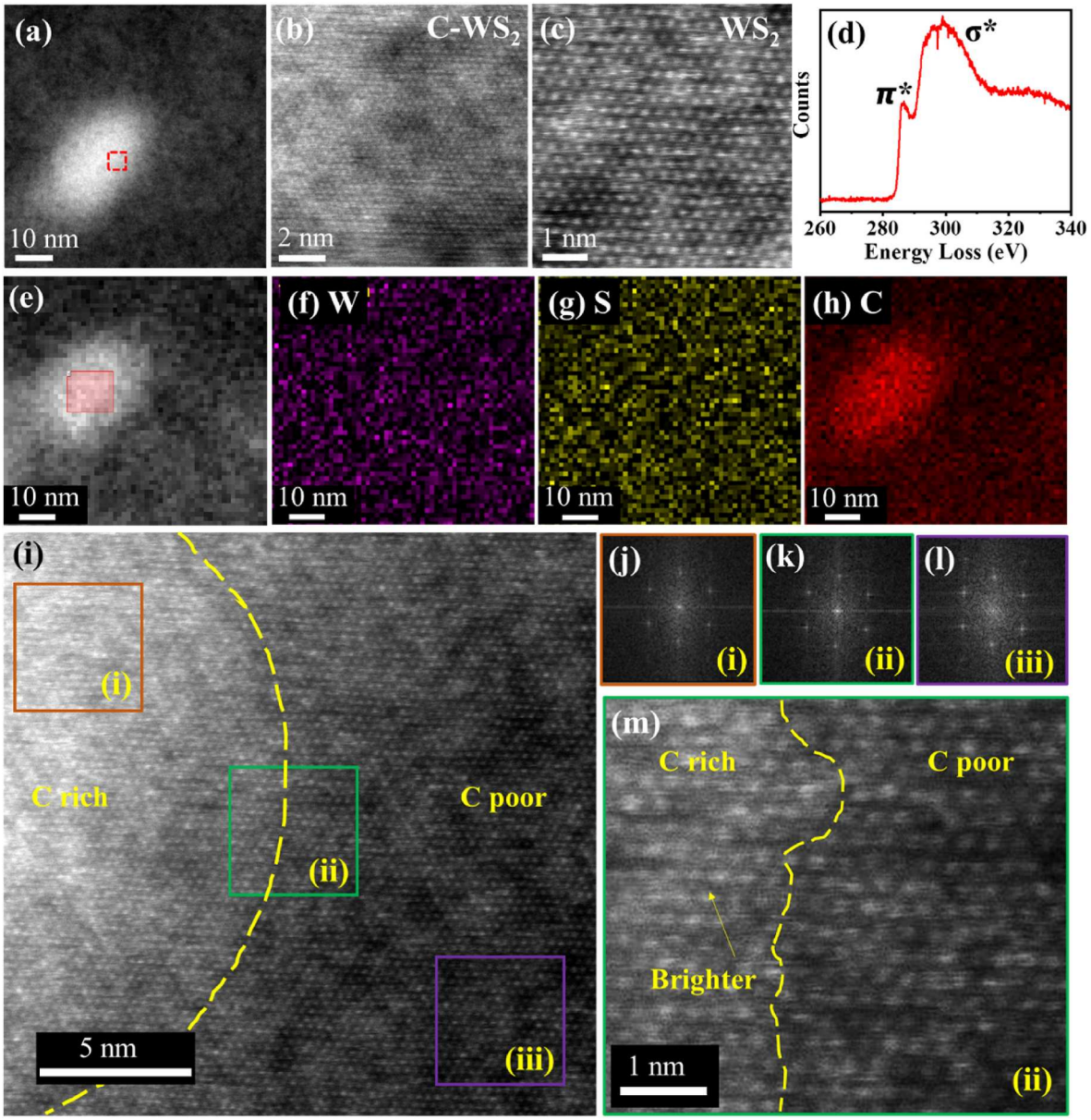

Fig. 2. (a) STEM image of a single C-pattern. (b) and (c) show the high-resolution STEM-HAADF images of marked C-WS_2 region and WS_2 region away from the C pattern respectively. (d) EELS spectrum of the patterned region. (e) STEM image of the C-pattern and the corresponding elemental mapping is shown in the next three images. (f) W (g) S (h) C. (i) STEM image of C-WS_2 interface. (j-l) FFT obtained from three marked regions. (m) Magnified image of region marked with green square in (i). (A colour version of this figure can be viewed online.)

significant difference was found in the C signal at ~1371.3 cm^{-1} (D) and ~1554.5 cm^{-1} (G), which was present only at the patterned site [36,43,44]. The G peak and D peak in Raman spectroscopy are caused by the relative motion of sp^2 carbon atoms and breathing modes of rings, respectively. Amorphous C can contain a mixture of sp^3, sp^2, and sp^1 sites. The G mode of graphite has E_{2g} symmetry and involves the in-plane bond-stretching motion of pairs of C sp^2 atoms. This mode occurs at all sp^2 sites and has a frequency range of 1500–1630 cm^{-1}. The D peak is a breathing mode of A_{1g} symmetry that involves phonons near the K zone boundary and is only active in the presence of disorder [45,46]. The I(D)/I(G) ratio of 0.598 in the present case indicates an amorphous C nature [43]. LA(M) mode near ~175 cm^{-1} arising due to the presence of defects in both patterned and non-patterned regions of WS_2 monolayer. Generally, CVD-grown WS_2 are S-deficient which justifies the presence of LA(M) mode in WS_2 [18,47]. To compare the relative change in intensity of this defect mode, the intensity ratio of E'/LA(M) was calculated. The intensity ratios of E'/LA(M) before and after C-patterning are ~2.14 and ~1.96 respectively. The slight decrease in ratio may be due to the introduction of carbon on WS_2 [18]. At the initial stage, the intrinsic S defects from CVD growth can bind C atoms during the EBID process on WS_2. The similar observation was also reported by F. Zhang et al. where the intensity of LA(M) mode strengthens as more C is introduced on the pre-existing S vacancies of WS_2. However, possible effect of e-beam on defect creations cannot be striked out completely but the possibilities are very less at the low energy of e-beam. Two more sets of Raman spectra have been presented in Fig. 3c also demonstrate the presence of the E′ mode at the same position.

To examine the e-beam-induced changes in the optical properties of WS_2, PL spectroscopy was conducted. Initially, a PL line scan was performed, covering both patterned and non-patterned regions of WS_2, as shown in Fig. 3d. The inset of the scan depicted that from the distance range of 0–2.4 μm, the PL was negligible, which corresponds to the substrate. Then, a sharp increase in PL was observed due to monolayer WS_2, which has a direct band gap and strong PL emission. As the scan

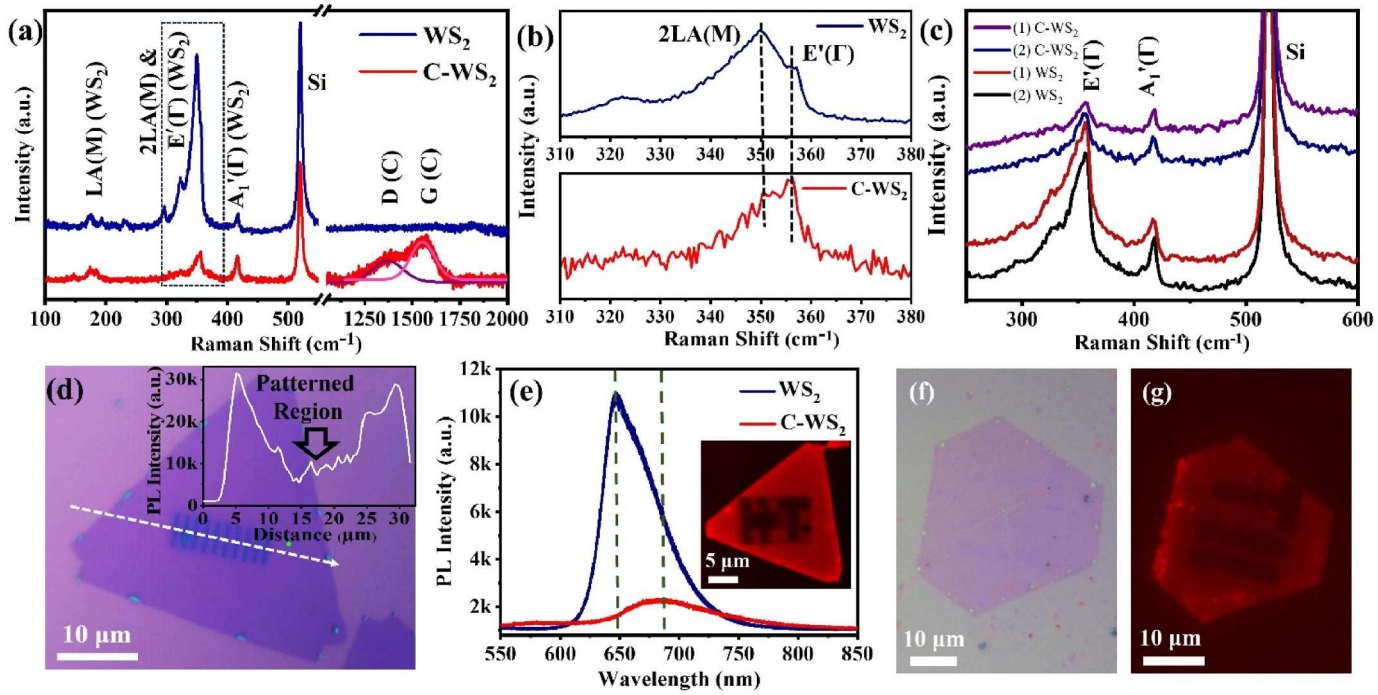

Fig. 3. (a) Comparative Raman spectra is taken from non-patterned WS_2 and C patterned WS_2 region. (b) Raman spectra of WS_2 region which is marked in previous figure. (c) Supporting Raman spectra (d) Optical image of patterned monolayer WS_2. The dotted line shows the region of the PL scan which is shown in the inset. (e) PL Spectra were taken at non-patterned and C-patterned WS_2 regions. The fluorescence image of patterned WS_2 is shown in the inset. (f) Optical image of WS_2 and (g) corresponding fluorescence images after flipping. (A colour version of this figure can be viewed online.)

reached the patterned region, PL started to decrease, indicating C-induced changes in the optical properties of WS_2. An average of ~3 times decrease in PL was observed in the patterned region, which was not zero due to the LASER's spot size (~1 μm) during measurement. Individual PL spectra were also collected on a non-patterned region and a patterned region of the same WS_2 flake as shown in Fig. 3e wherein a similar trend of decreased PL with ~4.7 times of quenching was observed from the patterned region. Additionally, a PL position shift of ~37.2 nm (~0.11eV) was observed. The deconvoluted PL spectrum is shown in Supplementary Fig. S6, where an increase in the contribution of the trions was observed after C patterning. In previous work, Ryan Selhorst et al. also found that the contribution of the trions increases after the e-beam functionalization of oxygen and hydroxyl groups on 2D materials by water vapor radiolysis [48]. A previous report by F. Zhang et al. mentioned the fusion of C into the S vacancy site lowering the energy of the valence band maximum to the Fermi level, causing a band gap reduction [18]. However, in our work it is not possible to clearly pin-point trion formation vs band-gap reduction as the mechanism for the red-shift of the PL.

The presented fluorescence imaging of patterned WS_2, in the inset of Fig. 3e, clearly distinguishes dark patterns in the form of "IIT" from the non-patterned WS_2 regions. We attempted to flip the patterned WS_2 upside down to check the role of deposited C which can mask the fluorescence of monolayer WS_2. Optical and confocal-fluorescence imaging after flipping is presented in Fig. 3f and 3g respectively. The flipped WS_2 revealed similar fluorescence tuning at the patterned site, indicating the mechanism of optical modulation beyond the C masking. However, the nanometer dimensionality of the patterns made them invisible in the optical image. This observation is similar to the work reported by A. Bora et al. in WS_2 quantum dots and C nanotubes, where charge transfer from WS_2 QD to CNT led to a non-fluorescent complex due to static quenching [49].

Specifically, quenching of fluorescence intensity at the patterned site was observed as shown in Fig. 3e. However, it must be noted that the central region of the letter "I" was magnified in FESEM, resulting in excessive e-beam exposure that affected the surrounding area. As a result, the region adjacent to the middle "I" appears dark in the fluorescence image. Nonetheless, this process may be leveraged as an optical method for writing on fluorescent materials. These findings suggest that patterned WS_2 could potentially be utilized to transfer confidential information, which could then be destroyed by overexposing it to an e-beam via the integration of C structures at the location of choice to selectively modulate the electronic structure and related optical emissions. To get further insights into the mechanism of fluorescence quenching at C-WS_2 contacts, KPFM imaging was employed. The surface potential or work function is a crucial intrinsic property of materials that is highly sensitive to the Fermi level. A Co/Cr coated AFM tip was used to scan the patterned WS_2 monolayer and inject 1 V of charge for the measurement. The KPFM potential image is shown in Fig. 4a, and the plot of the line drawn over it is shown in Fig. 4b. The plot shows three potential regions: the first corresponds to the SiO_2/Si substrate with a surface potential of ~280–300 mV, followed by a decrease in potential towards the WS_2 region with an average difference of ~48.0 mV between the substrate and monolayer WS_2. The non-patterned WS_2 region has a surface potential of ~245 mV, while the surface potential drops to a minimum at the C-pattern. A change in surface potential was observed around the area near the patterned region as compared to the non-patterned region. The average surface potential difference between the non-patterned WS_2 and C-patterns is ~95.6 mV. As surface potential and work function have an inverse relation, the charge carriers can flow from WS_2 to C due to the difference in surface potential. Since the work function is related to the measure of how tightly the electron is bound to the system, the charge transfer happens from WS_2 with a lower work function to C with a higher work function. This flow of charge carriers can also be attributed to the PL quenching mechanism in specific locations of monolayer WS_2 where C pattern is deposited. The KPFM results support the PL quenching mechanism by demonstrating that the charge transfer hinders the recombination process in WS_2, leading to poor emission. High-resolution AFM and KPFM were used to determine the precise variation in the patterned region. Fig. 4c shows the AFM height

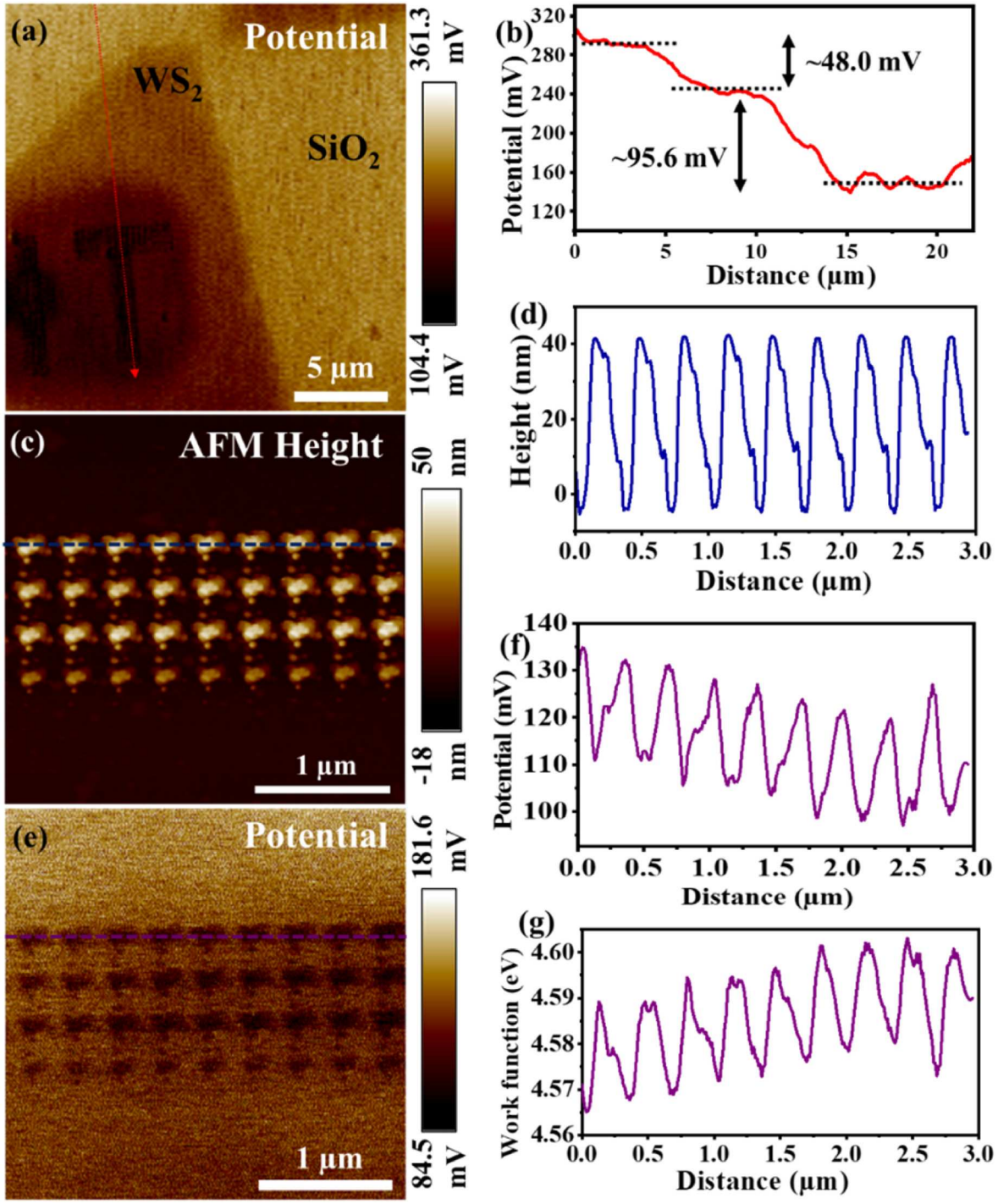

Fig. 4. Surface potential analysis using KPFM is shown. (a) KPFM image of patterned WS_2 monolayer is shown. (b) Line profile showing the surface potential across the line marked. (c) A High-resolution AFM height image of the pattern and (d) corresponding height profile is shown. (e) A high-resolution KPFM image of the same patterned region is shown along with (f) potential and (g) work function plots of the marked region. (A colour version of this figure can be viewed online.)

image of the dot pattern and its corresponding plot is presented in Fig. 4d. The average height for this specific pattern was approximately ~43.8 nm with a spacing of around 0.3 µm between each point. A high-resolution KPFM image at the patterned site is demonstrated in Fig. 4e, and the plot of surface potential modulation in the marked region is illustrated in Fig. 4f. The high-resolution potential plot displays a periodic variation, and the corresponding work function of the region is plotted in Fig. 4g. Typically, an increase in V_{CPD} indicates a lower work function (n-doping), while a decrease in V_{CPD} corresponds to an increase in work function (p-doping). In the context of C patterning on WS_2, Fig. 4a shows a decrease in V_{CPD} (an increase in work function), indicating p-doping in the patterned region. Previous studies have also reported p-type doping of WS_2 with the introduction of C via doping and the EBID process [18,48]. However, for p-type doping, the introduction of C in the WS_2 lattice is not necessary. The contact between the C nanostructure and WS_2 causing electron transfer from WS_2 to C can also contribute for p-type doping effect in WS_2.

The work function of material [$\varphi_{(Material)}$] is related to measured surface potential difference also known as contact potential difference (V_{cpd}) by the following relation.

$$\varphi_{(Material)} = \varphi_{(Tip)} - e.V_{cpd}$$

Where $\varphi_{(Tip)}$ denotes the work functions of the tip which was calculated to be 4.7 eV and e is the electronic charge [50]. The observed work function of the C-pattern is ~0.02 eV more than the WS_2 region, which is present between the two C-spot. This trend is similar to the mechanism suggested in an earlier report [49]. Here, C and WS_2 are already coupled with each other, and their fermi levels are also in alignment. Due to this, the difference in work function (after contact: 0.02 eV) is less compared to the value when direct contact was not present (0.095 eV). Hence a modulation in the electronic structure of the WS_2 region in close proximity with the C structure is confirmed and forms a platform for engineering the optical properties with good spatial control.

It is worth noting that such optical modulation has been previously reported by Jingang Li et al., for patterned C on WSe_2 [8]. The revelation made by the authors is that the presence of defects and oxidized states in 2D-TMDCs result in proficient C-H activation and chemical reactions. Moreover, the ability to activate C-H bonds in specific locations using light enables the optical printing of luminescent C dots onto solid surfaces. Weiwei Zhao et al. also showed data storage and encryption on monolayer WS_2 by using a focused LASER beam [27]. By utilizing ozone functionalization and scanning a focused laser beam, precise control of PL emission was achieved, which enables the realization of the write-in. The fluorescence contrast facilitates the visual decryption and reading-out of information [27]. We also utilized the PL engineering observed by C-WS_2 integration for writing the codes on WS_2 and showing the application in data encryption. The process of data encryption is shown in three steps as discussed in the next paragraph.

Fig. 5 illustrates the scheme utilized in optical encryption. In this study, Fig. 5a and 5b showcase the optical and FESEM image of CVD-grown WS_2. The corresponding PL intensity mapping is shown in Fig. 5c. Initially, the fluorescence of WS_2 was uniform throughout the entire sample. Moving on, selective e-beam exposure was applied to WS_2 to write symbols of choice, as demonstrated by marking "IIT" over two flakes. The code writing on WS_2 is step 1. Fig. 5d and 5e depict the optical and FESEM image of patterned WS_2 and the corresponding PL intensity mapping is shown in Fig. 5f. The written code can be easily captured due to the high contrast in the fluorescence image while remaining invisible under a visible light microscope. The reading and capturing of written code constitute the step 2. In the final step-3, overexposure inside FESEM was performed and the imposed changes are further captured by optical and FESEM images presented in Fig. 5g and 5h. Fig. 5i demonstrates an almost complete loss of PL in the overexposed region. Here with overexposure C structures formed everywhere in the selected region which hide the written code. By following these three steps, data entry, encryption, and deletion can be achieved. With the naked eye and optical microscope, these codes are undetectable due to their small feature size, making data confidential and at the same time remain accessible only via fluorescence and FESEM imaging. It may be noted that, the patterning process is highly dependent upon the exposure time of e-beam on sample. During the process of locating the same area, sample focusing, capturing images and zooming in and out, the area of interest receives greater interaction with the e-beam. Consequently, C deposition in the form of thin film occurs over the designated area leading to a small reduction in the PL values observed in Fig. 5c and 5f. However, the observed PL intensity change between the bare WS_2 and patterned WS_2 is very small. For example, difference in the PL intensity between bare WS_2 and patterned WS_2, recorded away from the patterned area is ~2–3K. The same difference obtained from the pre and post patterned region is ~25K.

The PL position mapping was captured at each step of data encryption along with the PL intensity mapping, as illustrated in Supplementary Fig. S7. Although fluorescence imaging is faster and less expensive than PL mapping, it lacks the sensitivity and resolution of the latter. Therefore, all steps of data encryption were also studied with fluorescence imaging and presented in Supplementary Fig. S8. In fluorescence imaging, the intensity must be sufficiently high to detect data. However, in PL mapping, small intensity difference can also be detected.

Optimization of the size of these patterns relies heavily on the parameters utilized in FESEM. The key parameters include magnification, spot size, acceleration voltage, and duration of irradiation. Throughout the experiments, a consistent writing area of approximately 3 × 3 μm^2

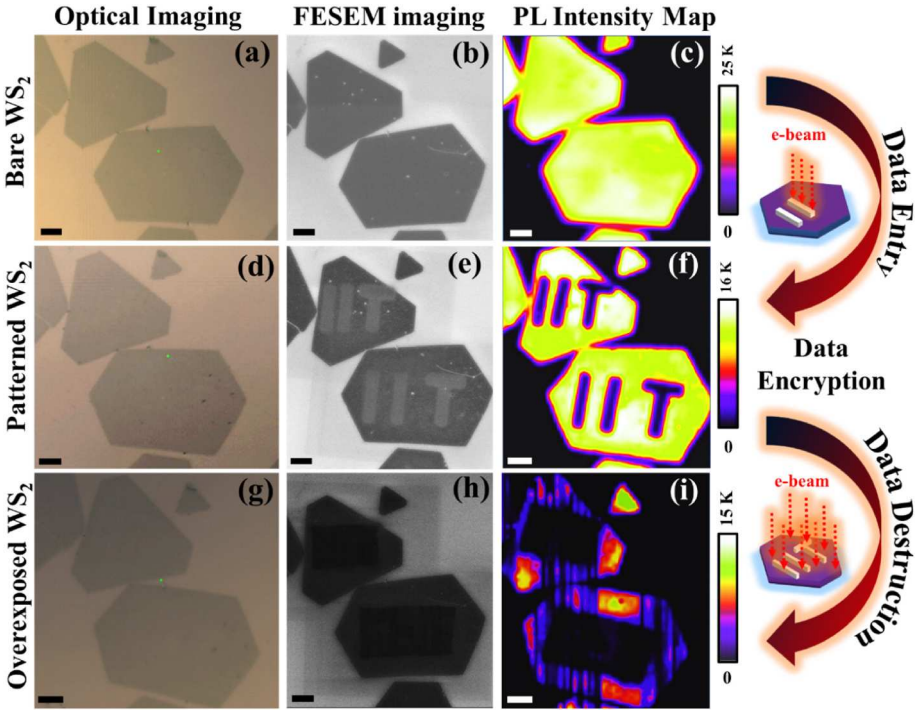

Fig. 5. (a) Optical, (b) FESEM, and (c) PL intensity mapping of bare WS_2. (d) Optical, (e) FESEM, and (f) PL intensity mapping of as patterned-WS_2. (g) Optical, (h) FESEM, and (i) PL intensity mapping of overexposed-WS_2. The scale bar is 5 μm for all. (A colour version of this figure can be viewed online.)

was maintained. To examine the impact of each parameter, one parameter was adjusted at a time while keeping the remaining parameters constant. For calculating the average values, the first point with max height was excluded from taking average values.

Firstly, magnification was varied to check its effect on patterns (Fig. 6). Here 10 kV, spot size 3, and 3 × 3 μm^2 area were kept as constant parameters. The patterning was carried out at 6500X, 8500X, 10000X, 12000X, 15000X, 35000X and 50000X magnifications (Fig. 6a–d). The AFM height plots from marked lines are presented in Fig. 6e and 6f. The AFM image of patterning performed at 50000X magnification is shown in Supplementary Fig. S9. The high-magnified AFM image of the same flake is shown in Fig. 1e where the minimum size of patterns was presented. At lower magnifications, the C patterns are larger in size and at more distance from each other. We found that the lateral feature size was highly dependent on magnification. By increasing the magnification, nanoparticle and even quantum structures can be achieved. In a particular area of writing, with an increase in magnification, the number of points was increased. Simultaneously, due to the increase in the density of structures, the distance between them decreases. The capability of dense nanoscale patterning is feasible within a height range of 2–3 nm. The variation of the width of the C-structure with magnification is plotted in Fig. 7a. As the area of writing is kept constant and with an increase in magnification, a greater number of points are formed so the e-beam is spending less interaction time per point.

To investigate the impact of exposure time, we conducted a patterning experiment while keeping all parameters constant except for time (10 kV, Spot Size 3,10000 magnification, pressure 3.32 e^{-3} Pa). The resulting optical image, as shown in Supplementary Fig. S10a, illustrates clear differences in the visibility of the patterns. Specifically, the patterns formed at 2000 s are the darkest and most easily identifiable, followed by those at 1000 s. The mildest patterning among these three is observed at 500 s, and patterns formed for just a few seconds are not visible under an optical microscope. Our observations indicate that the duration of exposure is directly related to the vertical as well as lateral growth of nanostructures (Fig. 7b).

The Supplementary Figs. S11 and S12 illustrates the effect of variation in spot size. Specifically, for spot sizes up to 3, the vertical height of the nanostructures increased whereas the further increase of spot size was found to decrease the height (Fig. 7c). The width of the C-structure was found to increase with spot size.

Fig. 7d highlights how the acceleration voltage impacts the vertical height and width of the nanostructure. The detailed AFM images are shown in Supplementary Fig. S13. As per the results, when the acceleration voltage of the e-beam is under 10 kV, the height of the structure tends to increase. However, once the acceleration voltage crosses that threshold, it begins to damage the nanostructure, causing a decrease in height. The systematic height variation with respect to the acceleration voltage can be seen from the AFM height profiles of patterned C structures shown in Supplementary Fig. S14. Whereas width was found to first decrease and then increase with acceleration voltage. The damaged C structures with lower heights resulted at 18 kV and 20 kV are shown in Supplementary Fig. S15. Notably, exposure time, accelerating voltage, and spot size does not affect the number of points or lateral distance within an area while magnification shows the controllability of the number of points and lateral distance in the pattern. The demonstrated controllability of feature size in the EBID process of C patterning on 2D materials on selected locations is relevant for modulating the fluorescence towards photonic, optoelectronic, and optical encoding applications. Similar work was also demonstrated on MoS_2 multilayers which resulted in a similar pattern formation as shown in Supplementary Fig. S16.

4. Conclusions

In summary, we harnessed the process of EBID of C nanostructures on WS_2 monolayer with high spatial control and precision. Site-specific integration of C nanostructures onto WS_2 monolayer with an in-depth analysis of various parameters such as magnification, time, spot size, and acceleration voltage on the C pattern has been demonstrated successfully. The atomic-level interface has been studied using STEM-HAADF imaging and EELS analysis while the modulation of properties including fluorescence/PL quenching and emission redshift at the C-WS_2 interface have been investigated. The remarkable difference in PL emission intensity and work function observed in patterned C-WS_2 suggest that the band structure of this semiconducting material can be adjusted through e-beam patterning with a high spatial resolution of a few nanometres. Finally, the work has demonstrated the ability to perform data encryption using EBID, with overexposure of the e-beam being used to showcase data destruction.

CRediT authorship contribution statement

Deepa Thakur: Conceptualization, Methodology, Data curation, Formal analysis, Investigation, Writing - original draft, Writing - review & editing. **Pawan Kumar:** Data Curation, Writing - review & editing. **Arjun Barwal:** SEM discussion. **Deep Jariwala:** Conceptualization, Resources, Supervision, Validation, Writing - review & editing. **Erich**

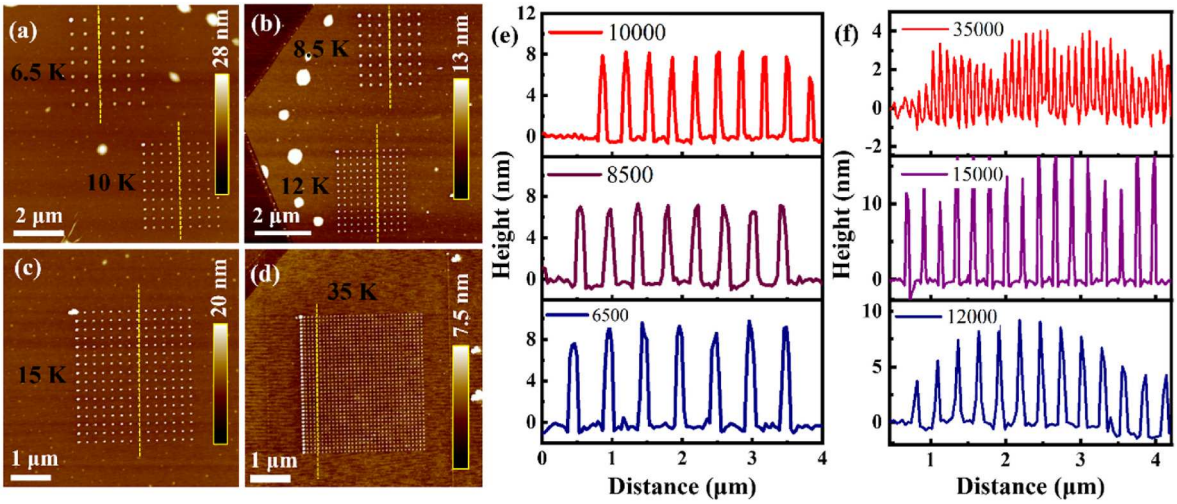

Fig. 6. AFM scan showing patterning performed with variation in magnification. AFM scan of the pattern performed at magnifications of (a) 6500 and 10000, (b) 8500 and 12000 (c) 15000, and (d) 35000. Line plots from these patterned regions are shown in figure (e-f). (A colour version of this figure can be viewed online.)

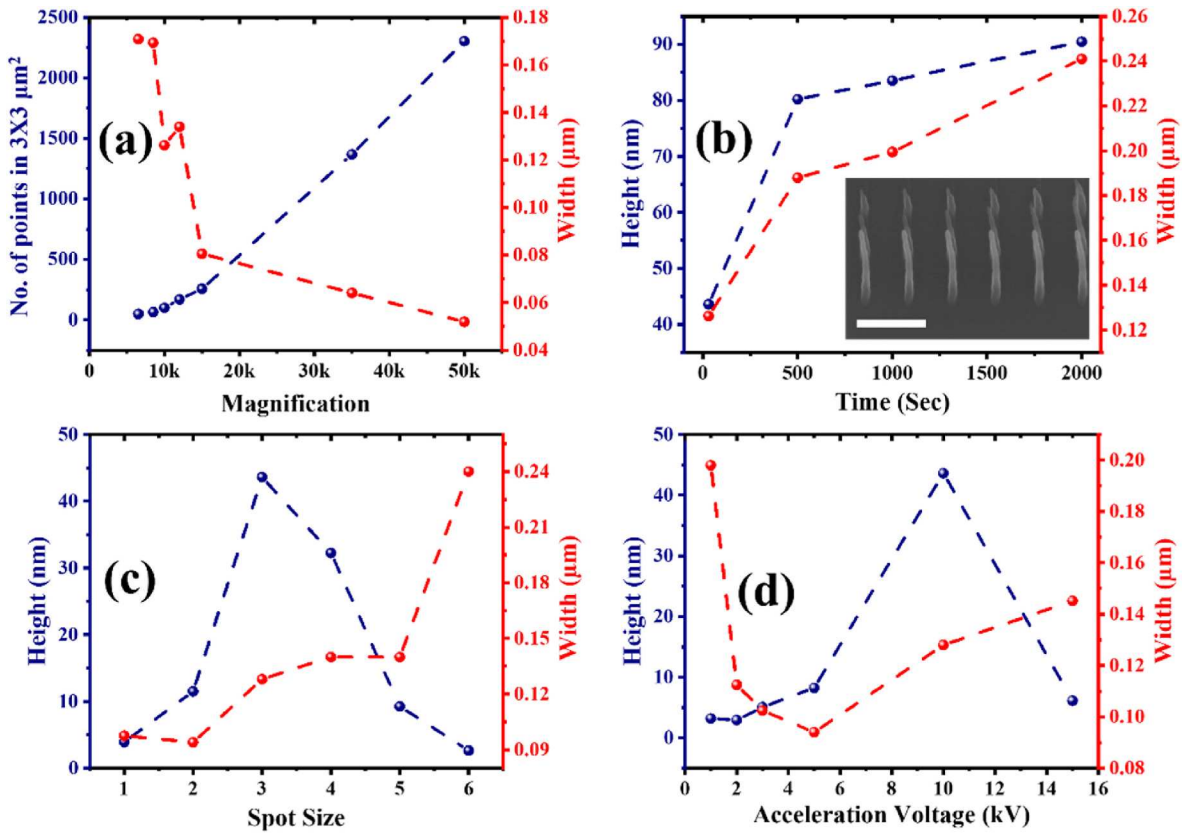

Fig. 7. Average size variation of C-structures as a function of FESEM operational parameters: (a) magnification, (b) exposure time (c) spot size, and (d) acceleration voltage. The scale bar is 500 nm in the images shown in the inset of (b). (A colour version of this figure can be viewed online.)

Stach: Supervision, Writing - review & editing. **Viswanath Balakrishnan:** Conceptualization, Supervision, Funding acquisition, Project administration, Resources, Validation, Writing - review & editing.

Declaration of competing interest

The authors declare that they have no known competing financial interests or personal relationships that could have appeared to influence the work reported in this paper.

Acknowledgments

We would like to express our gratitude to the "Department of Science and Technology- Innovation in Science Pursuit for Inspired Research" program (DST-INSPIRE, IF-180717) and Ministry of Education (STARS/APR2019/NS/654/FS) for providing a doctoral fellowship to Deepa Thakur and financial support for the project respectively. We also thank "Advanced Materials and Research Centre" (AMRC) at IIT Mandi for providing the necessary characterization facilities. Additionally, we extend our appreciation to Prof. Kamanio Chattopadhyay and Prof. N. Ravishankar for their valuable inputs on EBID. P.K., D.J., and E.A.S acknowledge primary support for this work from the National Science Foundation (DMR-1905853) and partial support from the University of Pennsylvania Materials Research Science and Engineering Center (MRSEC) (DMR-1720530), in addition to the usage of MRSEC supported facilities.

Appendix A. Supplementary data

Supplementary data to this article can be found online at https://doi.org/10.1016/j.carbon.2023.118339.

References

[1] M. Mohl, A.R. Rautio, G.A. Asres, M. Wasala, P.D. Patil, S. Talapatra, K. Kordas, 2D tungsten chalcogenides: synthesis, properties and applications, Adv. Mater. Interfac. 7 (2020), 2000002, https://doi.org/10.1002/admi.202000002.
[2] W. Zhang, Q. Wang, Y. Chen, Z. Wang, A.T.S. Wee, Van der Waals stacked 2D layered materials for optoelectronics, 2D Mater. 3 (2016), 022001, https://doi.org/10.1088/2053-1583/3/2/022001.
[3] Q.H. Wang, K. Kalantar-Zadeh, A. Kis, J.N. Coleman, M.S. Strano, Electronics and optoelectronics of two-dimensional transition metal dichalcogenides, Nat. Nanotechnol. 7 (2012) 699–712, https://doi.org/10.1038/nnano.2012.193.
[4] K.S. Novoselov, A. Mishchenko, A. Carvalho, A.H. Castro Neto, 2D materials and van der Waals heterostructures, Science (80-) 353 (2016) aac9439, https://doi.org/10.1126/science.aac9439.
[5] P. Lu, X. Wu, W. Guo, X.C. Zeng, Strain-dependent electronic and magnetic properties of MoS2 monolayer, bilaye, nanoribbons and nanotubes, Phys. Chem. Chem. Phys. 14 (2012) 13035–13040, https://doi.org/10.1039/c2cp42181j.
[6] Y. Ye, Z.J. Wong, X. Lu, X. Ni, H. Zhu, X. Chen, Y. Wang, X. Zhang, Monolayer excitonic laser, Nat. Photonics 9 (2015) 733–737, https://doi.org/10.1038/nphoton.2015.197.
[7] D. Thakur, P. Kumar, M. Sabarigresan, R. Ramadurai, V. Balakrishnan, Layer number dependent optical and electrical properties of CVD grown two-dimensional anisotropic WS2, Surface. Interfac. 26 (2021), 101308, https://doi.org/10.1016/j.surfin.2021.101308.
[8] J. Li, H. Li, H. Zhu, T. Zhang, Y. Gu, Z. Wu, S. Huang, Light-driven C-H Bond Activation Mediated by 2D Transition Metal Dichalcogenides, 2022, 07902. ArXiv: 2208.
[9] H. Nan, Z. Wang, W. Wang, Z. Liang, Y. Lu, Q. Chen, D. He, P. Tan, F. Miao, X. Wang, J. Wang, Z. Ni, Strong photoluminescence enhancement of MoS2 through defect engineering and oxygen bonding, ACS Nano 8 (2014) 5738–5745, https://doi.org/10.1021/nn500532f.
[10] S. Butun, S. Tongay, K. Aydin, Enhanced light emission from large-area monolayer MoS2 using plasmonic nanodisc arrays, Nano Lett. 15 (2015) 2700–2704, https://doi.org/10.1021/acs.nanolett.5b00407.
[11] Z.Q. Wu, J.L. Yang, N.K. Manjunath, Y.J. Zhang, S.R. Feng, Y.H. Lu, J.H. Wu, W. W. Zhao, C.Y. Qiu, J.F. Li, S.S. Lin, Gap-mode surface-plasmon-enhanced photoluminescence and photoresponse of MoS2, Adv. Mater. 30 (2018) 1–7, https://doi.org/10.1002/adma.201706527.
[12] L. Chu, Z. Li, H. Zhu, R. Li, F. Ren, F. Chen, Surface plasmon enhanced photoluminescence of monolayer WS2 on ion beam modified functional substrate, Appl. Phys. Lett. 118 (2021), https://doi.org/10.1063/5.0054333.

[13] A. Yang, J.C. Blancon, W. Jiang, H. Zhang, J. Wong, E. Yan, Y.R. Lin, J. Crochet, M. G. Kanatzidis, D. Jariwala, T. Low, A.D. Mohite, H.A. Atwater, Giant enhancement of photoluminescence emission in WS2-two-dimensional perovskite heterostructures, Nano Lett. 19 (2019) 4852–4860, https://doi.org/10.1021/acs.nanolett.8b05105.
[14] D. Thakur, Y. Sato, M. Sabarigresan, R. Ramadurai, V. Balakrishnan, Enhanced optical emission at MoS2-WS2 heterostructure interface with n-N junction, Appl. Surafce Sci. 606 (2022), 154923, https://doi.org/10.2139/ssrn.4179178.
[15] A. do Nascimento Barbosa, C.A.D. Mendoza, N.J.S. Figueroa, M. Terrones, F. L. Freire Júnior, Luminescence enhancement and Raman characterization of defects in WS2 monolayers treated with low-power N2 plasma, Appl. Surf. Sci. 535 (2021), 147685, https://doi.org/10.1016/j.apsusc.2020.147685.
[16] F. Bozheyev, R. Nemkayeva, N. Guseinov, M. Kaikanov, A. Tikhonov, Photoluminescence quenching of WS2 nanoflakes upon Ga ion irradiation, J. Lumin. 217 (2020), 116786, https://doi.org/10.1016/j.jlumin.2019.116786.
[17] C. Ma, J. Yan, Y. Huang, G. Yang, Photoluminescence manipulation of WS 2 flakes by an individual Si nanoparticle, Mater. Horiz. 6 (2019) 97–106, https://doi.org/10.1039/c8mh01072b.
[18] F. Zhang, Y. Lu, D.S. Schulman, T. Zhang, K. Fujisawa, Z. Lin, Y. Lei, A. Laura Elias, S. Das, S.B. Sinnott, M. Terrones, Carbon doping of WS2 monolayers: bandgap reduction and p-type doping transport, Sci. Adv. 5 (2019), https://doi.org/10.1126/sciadv.aav5003 eaav5003.
[19] V. Carozo, Y. Wang, K. Fujisawa, B.R. Carvalho, A. McCreary, S. Feng, Z. Lin, C. Zhou, N. Perea-López, A.L. Elías, B. Kabius, V.H. Crespi, M. Terrones, Optical identification of sulfur vacancies: bound excitons at the edges of monolayer tungsten disulfide, Sci. Adv. 3 (2017), 1602813, https://doi.org/10.1126/sciadv.1602813.
[20] K.A. Cochrane, T. Zhang, A. Kozhakhmetov, J.H. Lee, F. Zhang, C. Dong, J. B. Neaton, J.A. Robinson, M. Terrones, A.W. Bargioni, B. Schuler, Intentional carbon doping reveals CH as an abundant charged impurity in nominally undoped synthetic WS2 and WSe2, 2D Mater. 7 (2020), 031003, https://doi.org/10.1088/2053-1583/ab8543.
[21] M. Aghajanian, B. Schuler, K.A. Cochrane, J.H. Lee, C. Kastl, J.B. Neaton, A. Weber-Bargioni, A.A. Mostofi, J. Lischner, Resonant and bound states of charged defects in two-dimensional semiconductors, Phys. Rev. B 101 (2020), 081201, https://doi.org/10.1103/PhysRevB.101.081201.
[22] P.S. Kollipara, J. Li, Y. Zheng, Optical Patterning of Two-Dimensional Materials, Research, 2020, pp. 1–15, https://doi.org/10.34133/2020/6581250.
[23] D.S. Fox, Y. Zhou, P. Maguire, A. Oneill, C. Ócoileaín, R. Gatensby, A. M. Glushenkov, T. Tao, G.S. Duesberg, I.V. Shvets, M. Abid, M. Abid, H.C. Wu, Y. Chen, J.N. Coleman, J.F. Donegan, H. Zhang, Nanopatterning and electrical tuning of MoS2 layers with a subnanometer helium ion beam, Nano Lett. 15 (2015) 5307–5313, https://doi.org/10.1021/acs.nanolett.5b01673.
[24] H. Duan, D. Winston, J.K.W. Yang, B.M. Cord, V.R. Manfrinato, K.K. Berggren, Sub-10-nm half-pitch electron-beam lithography by using poly(methyl methacrylate) as a negative resist, J. Vac. Sci. Technol. B, Nanotechnol. Microelectron. Mater. Process. Meas. Phenom. 28 (2010) C6C58–C6C62, https://doi.org/10.1116/1.3501353.
[25] G. Yao, D. Zhao, Y. Hong, S. Wu, D. Liu, M. Qiu, Direct electron-beam patterning of monolayer MoS2 with ice, Nanoscale 12 (2020) 22473–22477, https://doi.org/10.1039/d0nr05948j.
[26] D. Zhao, A. Han, M. Qiu, Ice lithography for 3D nanofabrication, Sci. Bull. 64 (2019) 865–871, https://doi.org/10.1016/j.scib.2019.06.001.
[27] W. Zhao, S. Cai, X. Wei, T. Zheng, X. Xu, A. Zafar, H. Liu, T. Yu, J. Lu, Y. Chen, Z. Ni, The thinnest light disk: rewritable data storage and encryption on WS2 monolayers, Adv. Funct. Mater. 31 (2021), 2103140, https://doi.org/10.1002/adfm.202103140.
[28] D. Thakur, P. Kumar, V. Balakrishnan, Phase selective CVD growth and photoinduced 1T → 1H phase transition in a WS2 monolayer, J. Mater. Chem. C 8 (2020) 10438–10447, https://doi.org/10.1039/D0TC02037K.
[29] D. Thakur, M. Sharma, R. Vaish, V. Balakrishnan, WS2 monolayer for piezo–phototronic dye degradation and bacterial disinfection, ACS Appl. Nano Mater. 4 (2021) 7879–7887, https://doi.org/10.1021/acsanm.1c01202.
[30] T. Xu, X. Xie, K. Yin, J. Sun, L. He, L. Sun, Controllable atomic-scale sculpting and deposition of carbon nanostructures on graphene, Small 9 (2014) 1724–1728.
[31] J. Chen, G.H. Ryu, Q. Zhang, Y. Wen, K.L. Tai, Y. Lu, J.H. Warner, Spatially controlled fabrication and mechanisms of atomically thin nanowell patterns in bilayer WS2 using in situ high temperature electron microscopy, ACS Nano 13 (2019) 14486–14499, https://doi.org/10.1021/acsnano.9b08220.
[32] W.F. Van Dorp, C.W. Hagen, A critical literature review of focused electron beam induced deposition, J. Appl. Phys. 104 (2008), 081301, https://doi.org/10.1063/1.2977587.
[33] R. Walker, T. Shi, J. Robinson, Radiation effects on two-dimensional materials, Phys. Status Solidi A 213 (2016) 3065–3077, https://doi.org/10.1002/pssa.201600395.
[34] R.F. Egerton, P. Li, M. Malac, Radiation damage in the TEM and SEM, Micron 35 (2004) 399–409, https://doi.org/10.1016/j.micron.2004.02.003.
[35] P. Roediger, H.D. Wanzenboeck, G. Hochleitner, E. Bertagnolli, Evaluation of chamber contamination in a scanning electron microscope, J. Vac. Sci. Technol. B Microelectron. Nanom. Struct. 27 (2009) 2711, https://doi.org/10.1116/1.3244628.
[36] T. Bret, S. Mauron, I. Utke, P. Hoffmann, Characterization of focused electron beam induced carbon deposits from organic precursors, Microelectron. Eng. 78–79 (2005) 300–306, https://doi.org/10.1016/j.mee.2005.01.006.
[37] N. Silvis-Cividjian, C.W. Hagen, L.H.A. Leunissen, P. Kruit, The role of secondary electrons in electron-beam-induced- deposition spatial resolution, Microelectron. Eng. 61–62 (2002) 693–699, https://doi.org/10.1016/S0167-9317(02)00515-4.
[38] L.A.J. Garvie, A.J. Craven, R. Brydson, Use of electron-energy loss near-edge fine structure in the study of minerals, Am. Mineral. 79 (1994) 411–425.
[39] M. Bedewy, B. Viswanath, E.R. Meshot, D.N. Zakharov, E.A. Stach, A.J. Hart, Measurement of the dewetting, nucleation, and deactivation kinetics of carbon nanotube population growth by environmental transmission electron microscopy, Chem. Mater. 28 (2016) 3804–3813, https://doi.org/10.1021/acs.chemmater.6b00798.
[40] J. Bruley, D.B. Williams, J.J. Cuomo, D.P. Pappas, Quantitative near-edge structure analysis of diamond-like carbon in the electron microscope using a two-window method, J. Microsc. 180 (1995) 22–32, https://doi.org/10.1111/j.1365-2818.1995.tb03653.x.
[41] X. Shi, X. Li, Q. Guo, M. Zeng, X. Wang, Y. Wu, Ultrashort channel chemical vapor deposited bilayer WS2 field-effect transistors, Appl. Phys. Rev. 10 (2023), 011405, https://doi.org/10.1063/5.0119375.
[42] D. Thakur, M. Sharma, V. Balakrishnan, R. Vaish, Reusable piezocatalytic water disinfection activity of CVD-grown few-layer WS2 on sapphire substrate, Environ. Sci. Nano. 9 (2022) 805–814, https://doi.org/10.1039/d1en00926e.
[43] A. Ferrari, J. Robertson, Interpretation of Raman spectra of disordered and amorphous carbon, Phys. Rev. B - Condens. Matter Mater. Phys. 61 (2000) 14095–14107, https://doi.org/10.1103/PhysRevB.61.14095.
[44] D. Thakur, Y. Sato, V. Balakrishnan, Heteroatomic stitching of broken WS2 monolayer with enhanced surface potential, Nanoscale 15 (2023) 5274–5283.
[45] M.A. Pimenta, G. Dresselhaus, M.S. Dresselhaus, L.G. Cancado, Studying disorder in graphite-based systems by Raman spectroscopy, Phys. Chem. Chem. Phys. 9 (2007) 1276–1291, https://doi.org/10.1039/b613962k.
[46] J. Lynch, E. Smith, A. Alfieri, B. Song, C.Y. Chen, C. Kagan, H. Gu, S. Liu, L. Peng, S. Vangala, J.R. Hendrickson, D. Jariwala, Gate-Tunable Optical Anisotropy in Wafer-Scale , Aligned Carbon- Nanotube Films, 2023. ArXiv Prepr. ArXiv2304.08337.
[47] H. Rai, D. Thakur, D. Kumar, A. Pitkar, Z. Ye, V. Balakrishnan, N.N. Gosvami, Spatial variation in nanoscale wear behavior of chemical vapor deposited monolayer WS2, Appl. Surf. Sci. 605 (2022), 154783, https://doi.org/10.1016/j.apsusc.2022.154783.
[48] R. Selhorst, Z. Yu, D. Moore, J. Jiang, M.A. Susner, N.R. Glavin, R. Pachter, M. Terrones, B. Maruyama, R. Rao, Precision modification of monolayer transition metal dichalcogenides via environmental E-beam patterning, ACS Nano 17 (2023) 2958–2967, https://doi.org/10.1021/acsnano.2c11503.
[49] A. Bora, L.P.L. Mawlong, R. Das, P.K. Giri, Understanding the excitation wavelength dependent spectral shift and large exciton binding energy of tungsten disulfide quantum dots and its interaction with single-walled carbon nanotubes, J. Colloid Interface Sci. 561 (2020) 519–532, https://doi.org/10.1016/j.jcis.2019.11.027.
[50] P. Kumar, N.C. Verma, N. Goyal, J. Biswas, S. Lodha, C.K. Nandi, V. Balakrishnan, Phase engineering of seamless heterophase homojunctions with co-existing 3R and 2H phases in WS2 monolayers, Nanoscale 10 (2018) 3320–3330, https://doi.org/10.1039/c7nr08303c.